Predicting the dynamic impact behaviour of spray droplets on flat plant surfaces

M.A. Delele[1], D. Nuyttens[2], A. T. Duga[1], A. Ambaw[3], F. Lebeau[4], B.M. Nicolai[1], P. Verboven[1]

KU Leuven- University of Leuven, division BIOSYST-MeBioS, Willem de Croylaan 42, 3001 Heverlee, Belgium

[2]Institute for Agricultural and Fisheries Research (ILVO), Technology and Food Science Unit, Agricultural Engineering, Burgemeester Van Gansberghelaan 115, bus 1, 9820 Merelbeke, Belgium

[3]Stellenbosch University, South African Research Chair in Postharvest Technology, Stellenbosch, South Africa

[4]University of Liege, Gembloux Agro-BioTech, UMC, Passages des Déportés 2, 5030 Gembloux, Belgium

Abstract

The dynamic impact behaviour of water droplets on plant surfaces was investigated based on a multiphase computational fluid dynamics (CFD) model. The study was conducted using the Volume Of Fluid (VOF) approach. The static contact angle of water droplets on leaf surfaces of different plants (apple, pear, leek and cabbage) was measured and found to vary between 54.9 and 138.2°. Impact experiments were conducted by monitoring the flow and impact characteristics of water droplets on leaves in still air with a high speed camera. Droplets were generated by an agricultural flat fan spray nozzle moving across the leaf at constant speed. The nozzle produced droplets with diameters ranging from 20.6 up to 550.8 µm, and droplet velocity values near impact between 0.03 and 13.2 m s^{-1}. The CFD model was capable of predicting the observed dynamic

impact behaviour of droplets on the plant surfaces. The fate of the droplets after the impact process for adhesion, bouncing or splashing was accurately predicted for Weber numbers (We) in the range of 0.007 to 1096 and droplet Reynolds numbers (Re) between 5 to 8000. The process was highly dependent on surface and droplet flow characteristics during impact. Combinations of We, Re and Ohnesorge (Oh) numbers defined the droplet maximum spread factor, the number of secondary droplets generated as a result of the splashing process and the transition between the different impact outcomes. These criteria can then be used in field scale spray deposition and drift models to better understand agricultural spray operations.

Keywords: Spraying, Pesticide, CFD, Volume Of Fluid, Weber number

1. Introduction

In agriculture and horticulture, there are several areas where liquid droplets interact with plant surfaces, such as spraying of crop protection chemicals, irrigation and rainfall[1,2]. During application of crop protection chemicals, it is important to optimize the amount and uniformity of the on-target deposition while avoiding exceeding residue levels and minimizing run-off and drift with consequent environmental risks[3–5]. During irrigation, the amount of liquid that is intercepted by the plant canopy affects the performance of irrigation systems. Canopy interception is considered as one of the causes of water loss, and a reduction in plant transpiration rate due to canopy interception was also reported[6,7]. Leaves also intercept rainfall[8]. Intercepted rain can cause erosion of waxes from leaf surfaces and favours the development and dispersion of pathogens[9,10].

Understanding the impact characteristics of the liquid droplets on the plant surfaces helps in optimizing the required outputs and minimizing unwanted phenomena. The droplet-surface

interaction is a complex, dynamic multiphase process that determines the final fate of the impacted droplets[4]. At impact, a droplet first spreads due to its kinetic energy to the maximum possible spread area. Then due to the surface tension it starts to recoil back. This spread-recoiling process is associated with the loss of energy. Depending on the impact characteristics, droplets can adhere to the surface, bounce from the surface or shatter[11,12]. The influencing parameters include physical and chemical properties of the liquid, droplet size, velocity and impact direction, surface morphology of the plant surface and micro climate conditions[2,4,5,13,14].

Mathematical models have been presented as alternatives to the tedious and expensive field/laboratory studies for studying droplet impact on plants[5,12,15–21]. Few of these models are empirical[19], while most have been developed using physical principles[5,12,15,20-21]. Duga et al.[16,17] and Endalew et al.[18] developed a 3D canopy deposition model in the framework of a Lagrangian droplet tracking model which used a stochastic model to decide droplet deposition. No distinction was made between types of impact. Dorr et al.[5] presented a 3D model of droplet impact on cotton, wheat and chenopodium leaves that was capable of predicting the final fate of the impacted droplet, whether it was adhered, bounced or shattered. The model was based on scanned leaf images and applied a combined ballistic and random walk approach to model the movement of the droplets through the air. The model only predicted the final output of the impacting process without considering the impact dynamics, and assumed droplets impacting perpendicular to a horizontal leaf surface. Recently Massinon et al.[22] studied the variability of spray retention sing a 3-D model of a superhydrophobic leaf surface coupled with small and slanted leaves in relation to spray quality, applied volume, plant size and orientation and liquid formulation. The 3D architecture of a barley plant, the spray quality and the droplet impact behavior were measured and used as an

input to the model. Similar to the model of Dorr only the final fate of the impacted droplet was calculated.

Based on a review of literature, Glass et al.[23] concluded that CFD models have the potential to provide accurate predictions of pesticide droplet flow on leaf surfaces by taking into account the influences of each of the key parameters (surface topography and chemistry, initial spray deposition conditions, evaporation and multiple droplet spreading interactions). Multiphase computational fluid dynamic (CFD) models based on the Volume Of Fluid (VOF) approach have been used to study the dynamic behavior of droplet surface interactions in different systems[24–30], but not yet for droplet-plant interactions. VOF has the ability to dynamically capture the interface between the gas and the liquid phases and droplet surface impact characteristics by taking into account the properties of the liquid and the surrounding air, droplet impact characteristics and surface morphology.

The aim of this study was to develop and validate a 3-D two-phase CFD model of the dynamic impact behavior of water droplets on plant surfaces to improve predictive models of deposition and drift of agricultural spray operations. The study relied on experimental measurements to generate model parameters and for validation of the simulations. The model was applied to investigate the dynamics of the droplet impact process on different leaf surfaces of important agricultural and horticultural crops that require spray applications for pest management. The model was also used to predict the outcome of the impact in terms of adhesion, bouncing or splashing/shattering using agricultural spray nozzles that typically generate a wide range of values of important droplet characteristics such as droplet velocity and diameter. The used agricultural spray nozzle in this work produced water droplets with diameters between 20.6 and 550.8 µm, and droplet velocity values at impact between 0.03 and 13.2 m s^{-1}.

2. Materials and methods

2.1. Experimental studies

Different experiments were conducted to determine model parameters and for validation of the developed model. Validation experiments were conducted to capture the dynamics and the outcome of the impact process of the droplet on the plant surfaces. The experiments were conducted using distilled water.

2.1.1. Leaves

Experiments were conducted on leaves of apple (*Malus domestica*) and pear (*Pyrus communis*) trees, cabbage (*Brassica oleracea*) and leek (*Alium ampeloprasum var porrum*). The leaves of apple and pear were picked after harvest during the month of November from the orchards of KU Leuven in Rillaar, Belgium, and were considered old with respect to the seasonal growth stage of the tree. The study used only the green old leaves, which were stored in high humidity until the time of the experiment to avoid moisture loss. The cabbage and leek plants were collected from the Inagro research station in Rumbeke, Belgium. The plants were young and in good condition.

2.1.2. Leaf surface imaging and static contact angle measurement

Surface imaging of the leaves was conducted using Scanning electron microscopy (SEM) (Laboratory for Plant Systematics, K.U. Leuven, Belgium). Static contact angle of a water droplet on the plant surface was measured at the Department of Chemical Engineering of KU Leuven in Belgium using a KRÜSS Droplet Shape Analysis System DSA14 (KRÜSS GmbH, Hamburg,

Germany). Droplets of 2 to 6 μL were deposited carefully on the leaf surface using a small needle. When the equilibrium contact angle was reached, a picture of the droplet on the surface was taken using a camera. The wetting measurements have demonstrated that the contact angle hysteresis was fairly large for the studied surfaces, however in this study the static contact angle was solely considered. The shape of the droplet was calculated using droplet shape analysis software. Thereto, the drop contour line was identified and described using mathematical models that were available in the KRÜS droplet shape analysis program. The program compared the optically determined and the calculated contour line, the agreement between the two lines was taken as an important criteria for the accuracy of the contour analysis. The static contact angle was the angle formed between the outline tangent of the deposited droplet and the contact surface. A minimum of 10 repetitions were conducted. The results are given in Table 1, the old fruit tree leaves appeared more hydrophilic than those of the vegetables.

2.1.3. Characterization of droplet impact on leaves

The impact behaviour of the droplet on the plant surface was determined from images/videos that were captured using a high speed camera (Y4 CMOS, Integrated Design Tools, Florida, USA). The camera frame rate was set at 20000 frames/s. A leaf sample was placed in between the high speed camera and the light source (19LED, Integrated Design Tools, Florida, USA) (Fig.1). There was a distance of 0.50 m between the light source and target surface.

The velocity and diameter of the impacting droplets were determined using image processing with the software Motion Studio (Integrated Design Tools, Florida, USA). Droplet diameters (μm) were calculated from the product of the pixel number that was taken by counting the number of image pixels on a line from one side of the droplet through the centre of the droplet to the other, multiplied with the spatial resolution of the image (10.8 μm/pixel). The velocity of the droplets (m

136 s^{-1}) was calculated based on the droplet movement between the nth and nth + 10 frames, the spatial
137 resolution of the image and the frame rate of the camera.

138 A single droplet was generated using a droplet generator (Université de Liège, Gembloux,
139 Agro-Bio-Tech, Belgium) and used to validate the predicted result of the dynamic behaviour of
140 the impact of the water droplet on the plant surfaces. The droplet generator was working using a
141 piezoelectric element that can be driven with voltages up to 60 V[31]. The study captured the
142 dynamics of the impact process of the water droplet with a diameter of 310 μm and impact velocity
143 of 2.8 m s^{-1} on a cabbage leaf.

144 To investigate the output of the impact process, experiments were conducted using a
145 commercial spray nozzle. The target surface was fixed on a mounting stage under the moving
146 spray nozzle at a position where it was possible to capture a sufficient number of droplets in the
147 field of view. The nozzle was moving at a speed of 2 m s^{-1}, perpendicular to direction of the camera
148 and the light source; the speed representative of field spraying operations. A flat fan nozzle type
149 11004VS (TeeJet Technologies , Illinois, USA) at a liquid pressure of 3 bar was used. The nozzle
150 produced droplets with a wide spectrum of droplet size (20.6 to 550.8 μm) and impacting velocity
151 (0.03 and 13.2 m s^{-1}). A small strip of leaf, about 0.5 cm wide and 5 cm in length, was cut and
152 used as a target plant surface. Using bigger strips caused problems in terms of visualisation. In this
153 work, only droplets under perpendicular impact were considered.

154

155 **2.2. Impact dynamics and dimensionless numbers**

156 Dimensionless numbers were used to define the droplet maximum spread factor, the number
157 of secondary droplets generated as a result of the splashing process and the transition between the

different impact outcomes. The main dimensionless numbers that govern the dynamic impact process are the Weber number (*We*) and the Reynolds number (*Re*) [2,32,33]. *We* expresses the ratio of inertia to surface tension forces, *Re* gives the ratio of inertia to viscous forces. The Ohnesorge (*Oh*) number combines *We* and *Re* to provide a ratio of viscous to combined inertia and surface tension forces:

$$We = \frac{\rho D V^2}{\sigma} \tag{1}$$

$$Re = \frac{\rho D V}{\mu} \tag{2}$$

$$Oh = \frac{\mu}{(\rho \sigma D)^{\frac{1}{2}}} = \frac{We^{\frac{1}{2}}}{Re} \tag{3}$$

where ρ, σ, μ are the liquid density (kg m^{-3}), air-liquid surface tension (N m^{-1}) and liquid viscosity (Pa s) of the spray liquid, respectively. D (m) and V (m s^{-1}) are liquid drop diameter and impact velocity, respectively. In contrast to the Reynolds and Weber numbers, the Ohnesorge number does not depend on the hydrodynamics but solely on physicochemistry and geometry.

Mao et al.[34] presented an energy balance model of the droplet impact that is capable of calculating the maximum spread diameter (d_m) from the droplet diameter (D), static contact angle (θ), *We* and *Re*:

$$\left[\frac{1}{4}(1-\cos\theta) + 0.2\frac{We^{0.83}}{Re^{0.33}}\right]\left(\frac{d_m}{D}\right)^3 - \left(\frac{We}{12}+1\right)\frac{d_m}{D} + \frac{2}{3} = 0 \tag{4}$$

The model was developed for spreading and bouncing droplets on a flat surface over a wide value range of impact velocity (0.5-6 m s^{-1}), viscosity (0.001-0.1 Pa s), static contact angle (30-120°), droplet size (1500-3500 μm) and surface roughness. The contact angle of the droplets on rough surface was smaller than on smooth surface, however the rough and the smooth surfaces showed a similar general feature in terms of the maximum spread and bouncing behaviours. The study stated that the effect of surface roughness was introduced in the model using the contact angle of the rough surface not in the form of some other roughness parameters (like roughness height, roughness ratio, etc..). For values of $\frac{d_m}{D}$ less than 6, the agreement between the measured and predicted results was within a confidence level of 90%. Due to the flat disk assumption that was made in developing the model , there was a significant decrease in the accuracy of the model for lower impact velocities (less than 1 m s^{-1}). The model prediction was also compared to literature data[35–37] that were collected on a wide range of impact velocity (1.4-28 m s^{-1}), viscosity (0.001-0.296 Pa s), surface tension (0.025-0.073 N m^{-1}), static contact angel (34-100°) and droplet sizes (40-3700 μm). Predicted results showed an agreement to the literature data with a similar confidence level as above, so the equations appears valid for a wide range of *We* and *Re*.

Mundo et al.[38] conducted an extensive experimental study of droplet impact on a stainless steel surface for a smaller range of droplet diameter values (60-150 μm). They measured much higher values of impact velocity (12-18 m s^{-1}), and considered variations of surface tension (0.022-0.072 N m^{-1}), viscosity (0.001-0.0029 Pa s) and surface roughness (mean roughness heights of 2.8 and 78 μm). The study reported the surface profile data that showed the amplitude of surface roughness and the type of topographical features. The surface with the highest mean roughness height had a highly variable surface profile. Contact angles were not reported. The corresponding range of

impact *Re* and *We* values were 195-2694 and 94-2204, respectively. Compared to the smooth surface, rough surface produced a more irregular droplet deformation pattern. During splashing, rough surface produced secondary droplets which were smaller in mean diameter and narrower in droplet size distribution. The study developed an empirical relation that defined the boundary between deposition and splash regions using:

$$Oh \cdot Re^{1.25} = K \tag{5}$$

where K is constant and the critical value of K was reported to be 57.7. If the value of K is larger than 57.7, the droplet splashes, for lower values it deposits. It was later reported that the value of K increases with a decrease in surface roughness. Yoon et al.[39] reported a critical value of 152 for K during the impact of a water droplet on a paraffin wax surface. Vander Wal et al.[40] found critical values of 0.85 and 63, respectively for dry and wet aluminum surfaces. The study also reported a different exponent for *Re* of 0.609 and 1.17 for the dry and wet surface, respectively.

2.3. VOF model

The VOF method solves a single set of momentum equations while computing the volume fraction of each of the phases and resulting effective fluid properties throughout the computational domain. At the air-droplet interface, a continuum force model is applied to account for surface tension.

2.3.1. Governing equations

The continuity and momentum equations are:

$$\frac{\partial}{\partial t}(\rho)+\nabla\cdot(\rho\mathbf{v})=0 \tag{5}$$

$$\frac{\partial}{\partial t}(\rho\mathbf{v})+\nabla.(\rho\mathbf{v}\mathbf{v})=-\nabla p+\mu\nabla^2\mathbf{v}+\rho\mathbf{g}+\mathbf{F} \tag{6}$$

where t, $\mathbf{v}$, p and g are time, velocity, pressure and gravitational acceleration, respectively. ρ, μ, $\mathbf{g}$ and $\mathbf{F}$ are the apparent density, viscosity, gravitational acceleration and surface tension force per unit volume, respectively. Based on the value of the volume fraction (α_l) of the liquid water phase, the fluid properties and the flow variables in any computational cell represent either one of the phases or a mixture of the phases.

The apparent density and viscosity in each cell were calculated using:

$$\rho=\alpha_l\rho_l+(1-\alpha_l)\rho_a \tag{7}$$

$$\mu=\alpha_l\mu_l+(1-\alpha_l)\mu_a \tag{8}$$

where ρ_l and ρ_a are the density of liquid and air, respectively; and μ_l and μ_a are the viscosity of liquid and air, respectively. The interface between the liquid and the air phase was tracked by solving the continuity equation for the volume fraction of the liquid phase:

$$\frac{\partial}{\partial t}(\alpha_l)+\nabla\cdot(\alpha_l\mathbf{v})=0 \tag{9}$$

with

$$\alpha_a=1-\alpha_l \tag{10}$$

The surface tension force per unit volume ($\mathbf{F}$) was calculated using a continuum surface force model[41]. The model interprets surface tension as continuous, 3-D effect across an interface, rather than as a boundary value condition on the interface. For the two phase system:

$$\mathbf{F} = \sigma \frac{\rho k \nabla \alpha_l}{\frac{1}{2}(\rho_l + \rho_a)} \tag{11}$$

The curvature (k) is given by:

$$k = -(\nabla \cdot \mathbf{n}) \tag{12}$$

The unit normal $\mathbf{n}$ is given by:

$$\mathbf{n} = \frac{\nabla \alpha_l}{|\nabla \alpha_l|} \tag{13}$$

2.3.2. Numerical procedure

The simulations in this study were conducted using ANSYS Fluent 16.2 (ANSYS, Inc., Pennsylvania, USA). Three-dimensional rectangular computational domains were developed and discretized using an appropriate mesh size (Fig. 2). After conducting a mesh sensitivity study, the size of the mesh was decided to be smaller than the diameter of the droplet divided by 45. The size of the domain depends on the size of the droplet and its impact velocity. In order to capture all details of the impact, spreading and break-up process, droplets with higher diameter and impact speed required a larger domain size. The study analysed droplet sizes in the range of 50 to 800 µm and impact velocities of 0.1 to 10 m s^{-1}. Minimum contact surface sizes of 1 mm by 1 mm and a maximum size of 16 mm by 16 mm were used. Depending on the size of the droplets, uniform

mesh element sizes in the range of 2.5-30 µm (2.5 µm for 50 µm droplet and 30 µm for 800 µm) were used. The solution domains consisted of up to 12.5 million hexahedral elements.

The plant surface was taken as a flat no slip wall and the rest of the boundaries were defined as pressure outlets. To predict the contact behaviour of the droplet on the plant surface, the wall adhesion model of Brackbill et al.[41] was applied. In this model the contact angle of the droplet on the wall is used to determine the droplet surface normal in computational cells near the wall ($\mathbf{n} = \left(\mathbf{n}_t \sin\theta + \mathbf{n}_w \cos\theta\right)$, where $\mathbf{n_w}$ and $\mathbf{n_t}$ are the unit vectors normal and tangential to the wall, respectively. The dynamic boundary condition results in the adjustment of the curvature of the surface near the wall. The model input parameters that include the measured static contact angles of the droplets on the leaf surfaces, the viscosity and surface tension of the liquid are given in Table 1. Initially, the droplets were placed a small prescribed distance of 0.1 mm above the contact surface with an initial (impact) velocity (Fig. 2). Initially the surrounding air was assumed to have zero velocity and 101.3 kPa pressure, and it was considered as compressible gas.

A fractional step algorithm was used for pressure-velocity coupling. The continuity, momentum and volume fraction equations were solved using the PRESTO, QUICK and compressive method, respectively for spatial discretization. Time discretization used the first order implicit method. A time step size of 1×10^{-7} s was needed to capture the important features of the impact dynamics of the droplet on the plant surface. The selected mesh size and time steps fulfilled the criteria of the maximum Courant number ($\frac{V\Delta t}{\Delta x} \leq 0.25$) of the simulation that was set to be 0.25. V is the impact velocity (m s^{-1}), Δt is the time step (s) and Δx is the grid size (m). The calculations were performed on a 64-bit, Intel® Core™ i7-4790 CPU, 3.60 GHz, 32 Gb RAM, Windows 7 Professional computer and the CPU time of calculation was up to 76 h.

3. Results and discussion

3.1. Impact dynamics of the droplet with no splashing

The impact process of water droplets during collision on hydrophilic (late season apple leaf with a static contact angle of 54.7°) and hydrophobic (young cabbage leaf with a static contact angle of 138.2°) plant surfaces are shown in Fig. 3a and 3b, respectively, for 300 µm droplet impacting at 2 m s^{-1}. The droplet was impacting vertically on a horizontal surface (impact angle equal to 90°). This impact angle was considered throughout this study. The corresponding Weber and Reynolds numbers were 16.4 and 600, respectively. As the liquid droplet makes contact with the plant surface, it starts to spread radially and forms a lamella and rim. For this impact *We* and *Re* condition, droplets either deposited on the leaf or bounced from the surface. On hydrophilic plant surfaces (static contact angle < 90°), after recoiling and a series of oscillations the droplet reached its equilibrium position and deposited (Fig. 3a). This deposition showed that the droplet that impacted on an old apple leaf at *We* = 16.4 and *Re* = 600 did not have enough energy to overcome the adhesive force of the surface. On the hydrophobic plant surfaces (static contact angle > 90°), after recoiling the droplet bounced back from the surface (Fig. 3b). Such an impact on the hydrophobic young cabbage surface indicated that the droplet maintained enough kinetic energy to rebound after recoiling. For lower Weber numbers (*We* < 0.3) the droplet did not have enough energy to bounce back from hydrophobic plant surfaces.

The velocity distribution during the spreading and recoiling of the droplet after impact on the old apple leaf is given in Fig. 4a. After impact the liquid flow changes from vertical to radial during the spreading phase. As the spread progresses, there is a decrease in radial velocity. When it reaches the maximum possible spread diameter, it starts to recoil back and finally attains the

equilibrium state and adheres on the surface. The velocity distribution during the impact process of the droplet on the young cabbage leaf (Fig.4b) was different from that of the old apple leaf (Fig. 4a). During the bouncing stage, there was a generation of a relatively high upward velocity.

When the droplet impacted the surface, a certain amount of air was entrapped and generated a high pressure region around the centre of the impact (Fig. 5). The pressure of entrapped air caused a deformation on the air-liquid interface and formed a dimple on the droplet surface. It was reported that the change of droplet velocity from vertical to radial flow during the spreading phase was driven by the strong pressure gradient that was generated during the impact process[42,43]. As the spread progressed, there was a decrease in radial velocity and pressure (Fig. 4 and Fig. 5). For the 300 µm droplet impacting at 2 m s^{-1}, the entrapped air was shrinking with time and finally part of it was drained through the top surface of the spreading droplet. Thoroddsen et al.[44] presented an experimental study of the contraction behaviour of the air disk that was caught under a drop impacting onto a solid surface for a wide range of impact *We* (20-1500) and *Re* (5-30000) numbers. The size of the initial air disk was affected by the curvature of the droplet at the initial contact and the contraction speed of the air disk was independent of the wettability of the liquid.

For this impact velocity and droplet diameter, there was a similar pressure decay profile between old apple leaf and young cabbage leaf; there was no significant difference (at 95 % confidence interval) in peak pressure value. It is known that this phase of the impact process is dominated by the inertial forces that is determined by the impact velocity and droplet diameter[42,43,45]. van der Veen et al.[46] experimentally studied the behaviour of the entrapped air between the impacting droplet and hydrophobic micropatterned surfaces. The presence of the protruding pillars increased the pressure and central dimple height, however the height of the dimple was not affected by the pillar height. This shows that an explicit model of the surface

structure of the rough leaves could produce a significantly different pressure profiles between the two types of leaves. But such an explicit model will increase the complexity of the model and computational time.

Fig. 6 presents dimensionless characteristics of the droplet flow for the two cases, with D the initial droplet diameter, d the droplet spread diameter at time t, h the droplet height at the centre of the droplet at time t, τ the dimensionless time ($\tau = \frac{tV}{D}$) with V the (initial) impact velocity of the droplet. The maximum spread area of the droplet after impact was higher for the hydrophilic than the hydrophobic plant surface (compare Fig. 6a to Fig. 6b). For the 300 μm water droplet impacting at 2 m s^{-1}, the maximum spread diameter on the old apple leaf surface was 1.46 times higher than that of the young cabbage surface (Table 2). It took longer time for the droplet to reach the maximum spread area on hydrophilic surface than the hydrophobic surface. Up to the time it reached the maximum spreading rate, the spread rate ($\frac{d}{D}$) follows a power law relationship with the dimensionless time, with an exponent of 0.56 and 0.51 for old apple and young cabbage leaves, respectively ($r^2 > 0.98$).

During the early stage of the impact process there was a linear decrease of the droplet height, and gradually it attained the minimum height (film thickness) of the droplet (Figs 6c and 6d). This linear decrease in droplet height is due to the freefall of the top of the droplet[33]. During the recoiling period the height of the droplet started to increase from its minimum value and on the hydrophilic surface it showed considerable oscillations and finally reached to its equilibrium height (Fig. 6c). In the case of the hydrophobic surface, during the recoiling period the height of the droplet continuously increased till the droplets bounced back from the surface (Fig. 6d). The height of the

326 droplet during bouncing from the hydrophobic young cabbage surface was 5.1 times higher than
327 the height of the droplet that was deposited on the hydrophilic old apple leaf surface.

328 There was a good agreement between the maximum spread diameters that were calculated
329 using Eqn. (4) and predicted using the CFD model of this study (Table 2). For a 300 μm water
330 droplet impacting at 2 m s^{-1}, the deviation of the CFD model prediction result relative to the result
331 that was calculated using Eqn. (4) was 11.1, 8.5, 10.6 and 12.3 % for the old apple, old pear and
332 young cabbage and young leek leaf, respectively. The average deviation for wide ranges of impact
333 velocity (0.1-5 m s^{-1}) and diameter (50-800 μm) on an old apple and young cabbage surface that
334 resulted in either deposition or rebound of the impacted droplets was 13.8 and 11.6 %, respectively.
335 Note that for lower impact Weber number (< 2.7), Eqn. (4) does no give real solution for d_m. Using
336 Eqn. (4), it is thus possible to predict the maximum spread diameter for depositing and rebounding
337 droplet but it was impossible to know the dynamic behaviour and result of the impact process that
338 is rendered by the CFD simulations.

339 Table 2 shows that the maximum spread diameter of the droplet during impact was affected by
340 the wettability of the plant surface. Comparison was made between the results from two
341 hydrophilic (old apple leaf and pear) and two hydrophobic (young cabbage and leek) plant
342 surfaces. Within the hydrophilic plant surfaces, the relatively higher static contact angle decreased
343 the maximum spread diameter of the droplet and increased the equilibrium adhesion height of the
344 droplets (compare the maximum spread diameter on the apple and pear leaves). In the case of
345 droplets bouncing from hydrophobic surfaces, decreasing the static contact angle increased the
346 maximum spread diameter (compare the maximum spreading diameter on the young cabbage and
347 leek leaves).

348 *3.2. Impact dynamics of the droplet with shattering*

The predicted dynamic behaviour of a 300 µm water droplet during impact at a relatively high velocity (10 m s^{-1}) on a horizontal young cabbage leaf is presented in Fig. 7. The corresponding Weber and Reynolds numbers were 411 and 3000, respectively. Upon impact the droplet flattened quickly, expanding radially in the form of a sheet, and forming a lamella and rim. Similar to the no splashing case, upon impact the entrapped air generated a dimple and high pressure region (Fig. 8). In this case, the peak pressure was 2.9 times higher than the no splashing case. During this relatively high impact velocity, the entrapped air was contracted and the pressure decayed faster than in the no splashing case. This was in agreement to the report of Thoroddsen et al.[44]. Mandre et al.[47] reported that for a relatively high impact velocity the air dimple is responsible for the splashing of the droplet and the dimple height is affected by pressure of the surrounding gas and the impact velocity. It has been reported that even at very high impact velocity, the combined action of the gas layer and liquid surface tension stops the droplet from contacting the solid surface, rather the droplet spreads on a very thin film of air and emits capillary waves[47,48]. In this study due the relatively coarser mesh size (relative to the thickness of the air film), it was not possible to distinguish the expected very thin air film. According to Xu et al.[49], it is possible to control the splashing process by controlling the pressure of the surrounding gas. For a given impact velocity, decreasing the pressure of the surrounding gas supressed the splashing of the droplet and below a certain threshold pressure value the splashing was completely suppressed.

The lamella near the edge of the expanding sheet lifted up off the plant surface and formed a crown type section. During the spreading process the sheet further thinned while the rim thickened. Villermaux and Bossa[50] reported that the rim is gradually fed by incoming fluid from the sheet and is continuously stretched up to the equilibrium diameter. As the sheet expanded, perturbations were formed on the border, then the rim was destabilized and radial ligaments (fingers) were

formed. The ligaments were detached and formed small droplets. Compared to the droplet that adhered on the surface without shatter, the shattered small droplets covered a relatively larger area of the plant surface. Even for the hydrophobic plant surfaces most of these small droplets did not have the energy for bouncing rather adhered on the surface[12]. This shattering of droplet could be beneficial for instance in crop spraying applications by increasing the coverage area and uniformity of crop protection chemical deposition.

3.3. Comparison of predicted and experimentally observed droplet impact

The predicted and measured shape changes of a water droplet with a diameter of 310 μm and impact velocity of 2.8 m s^{-1} on a young cabbage leaf is presented in Figure 9. The conditions corresponded to a Weber and Reynolds number of 33.3 and 868, respectively. There was a visually good agreement between the changes in shape of the droplet during the spreading, recoiling and bouncing stages (compare Fig. 9a to 9b). In both cases, the maximum spreading diameter and bouncing occurred at about 0.15 ms and 0.55 ms, respectively. There was also a good agreement between the measured and predicted dimensionless droplet spread diameter and droplet height (Fig. 9c and 9d). For a given time after impact, the predicted height of the droplets during the recoiling and bouncing period was slightly higher than the measured one. It was reported that the use of dynamic contact angle instead of the static angle can improve the accuracy of the model during the receding phase[51]. The dynamic contact angle takes into account the hysteresis effect (which is neglected when static contact angle is assumed) that is often observed during the dynamic droplet impact process. The assumption of static contact angle did not have any influence on the prediction during the spreading phase of the impacted droplet when the process is dominated by inertia, but mainly during the receding phase when the process is dominated by surface tension and viscous forces.

The predicted and measured impact outcome after impact as a function of *We* and *Re* of the impacting droplet on cabbage and apple leaf surfaces are presented in Fig. 10. The model showed a clear transition from one impact behaviour to another, whereas there was some overlap in the measured results. This could be due to measurement errors on the exact droplet diameter, the inhomogeneous surface characteristics of the real leaf and impact velocity which was measured on 2D frames of an essentially 3D spray process. The measured and predicted critical Weber numbers for the transition from adhesion to bounce and from rebound to shatter for old apple, pear, leek and cabbage leaf leaves are given in Table 3. The model slightly over predicted the critical Weber number for the transition from adhesion to bounce/shatter, but slightly under predicted the critical Weber number for the transition from bounce to shatter. The critical Weber number for transition from adhesion/bounce to shatter was higher in hydrophilic (old apple and pear leaves) than hydrophobic (cabbage and leek leaves) plant surfaces, which was correctly predicted by the CFD model. From their study of droplet impact on surfaces of various wettability, Aboud and Kietzig[52] observed a similar lower splashing threshold value for hydrophobic surfaces compared to hydrophilic surfaces.

3.4. Defining the impact characteristics using dimensionless numbers

The droplet impact characteristics on the plant surfaces were defined using *We*, *Re* and *Oh* numbers. In this study simulations were conducted for different droplet diameters and impact velocities that produced *We* in the range of 0.007 to 1096 and *Re* in the range of 5 to 8000.

3.4.1. Maximum droplet spread factor

Fig. 11 shows the predicted (using CFD and Eqn. (4)) maximum spread factor ($\frac{d_m}{D}$) of the droplet as a function of *We* for adhered and rebounded droplets. The maximum spread factor of

the droplet on old apple leaf was higher than that of young cabbage leaf. The trend followed a power law relationship (r^2 = 0.92 for apple leaf and r^2 = 0.91 for young cabbage leaf) with exponents of 0.12 and 0.15 for the hydrophilic old apple and hydrophobic young cabbage leaves, respectively. From their study of water and mercury droplets impact on a super hydrophobic surface (static contact angle of 170°), Clanet et al.[53] found a similar power law relationship with an exponent of 0.25 between the droplet maximum spread factor and *We*. The result showed that the exponent of this power law relationship was affected by the properties of the impact surface.

For this range of *We* values (droplet impact velocity of 1-7 m s^{-1} and diameter of 50-800 μm) CFD predicted maximum spread factors were compared to the results that were obtained from Eqn. (4)[34] and on average there was a difference of 9.3 % and 10.1 % for the impact on old apple and young cabbage leaf surfaces, respectively. This relatively small difference showed that in addition to predicting the dynamic droplet impact behaviour the CFD model was also capable of predicting the maximum spread factor of water droplets on plant surfaces.

3.4.2. Number of secondary droplets

There was a linear correlation (r^2 = 0.93 for old apple leaf and r^2 = 0.99 for young cabbage leaf) between the number of secondary droplets (N_{sd}) after splashing and $We \cdot Re$ (Fig. 12). For given impact *Re* and *We* values, the number of secondary droplets generated during splashing on the hydrophilic apple leaf was lower than that of the hydrophobic cabbage leaf surface. From the droplet splashing study, Bussmann et al.[54] observed a decrease in the tendency of fingering with an increase in surface wettability (a decrease in contact angle). There was a power law relationship between the number of secondary droplets generated and $We \cdot Re$ with an exponent of 0.34 and 0.55 for the old apple and young cabbage leaves, respectively. According to Marmanis and

Thoroddsen[55] the number of fingers generated during the breakup process scaled with $We^{\frac{3}{16}}Re^{\frac{3}{8}}$. They stated that the number of fingers is weakly dependent on the surface tension and depends primarily on the inertial-viscous interaction. The result of this CFD study was fitted to this equation by assuming this scaling relationship of droplet fingers may work for the secondary droplets. However, compared to the proposed relationship it showed a relatively weaker correlation.

3.4.3. Transition between different impact outcomes

The predicted boundary lines between the different droplet impact outcomes on hydrophilic apple (adhesion and shatter) and hydrophobic cabbage (adhesion and bounce, bounce and shatter) leaves are given in Fig. 13. The boundary lines were expressed as a function of *Oh* and *Re* number in the form of Eqn (5). For the transition from adhesion to shatter for old apple leaf, the boundary line was defined by $OhRe^{1.25} = 42.95$. This means that a droplet that impacts with $OhRe^{1.25} < 42.95$ adheres to the surface while a droplet that impacts with $Oh\,\mathrm{Re}^{1.25} > 42.95$ splashes. In the case of cabbage leaf, the boundaries between adhesion and bounce and bounce and shatter were expressed as $OhRe^{1.25} = 2.63$ and $OhRe^{1.25} = 35.35$, respectively. Due to the relatively high contact angle, young cabbage leaf showed a relatively lower critical value of K during the transition from bounce to shatter. The critical value of K is dependent on surface properties of the plant surface and the values should be defined using independent studies. Mercer et al.[12] reported a similar conclusion about the dependence of the critical value of K on surface roughness and contact angle. The result shows there is a need to develop a better model equation that incorporates the effect of surface roughness and contact angle.

3.5. Relation between droplet impact characteristics and surface morphology of the leaves

460 The images of the SEM showed there is large difference between surface morphology of the
461 leaves of cabbage, leek, apple and pear (Fig. 14). The surface structure of the hydrophobic cabbage
462 leaf consisted of a number of protrusions/bumps which is affecting the surface wettability by
463 entrapping air between the droplet and the leaf surface. The presence of the grooves in the leek
464 leaves could create a difference in the spreading behaviour and contact angle of the droplet in the
465 parallel and perpendicular direction. The height of the protrusions on the surfaces of the
466 hydrophilic old apple and pear leaves was smaller than that of cabbage leave. Even within the same
467 leaf, inhomogeneity in surface structure was observed (it was more pronounced in the case of leek
468 leaf). This variation in surface structure could cause a variation in adherence/bounce behaviour on
469 the leaf surface. The size of the grooves on the leek leaf was around 20 μm that was less the
470 minimum diameter (50 μm) of the droplet that was considered in this study. Similarly the size of
471 the micro/nano protrusions on the other surfaces was lower than 50 μm.

472 This study showed that VOF model using measured static contact angle as an input parameter
473 gives a reasonably accurate result. It is known that surface roughness is highly related to contact
474 angle and its hysteresis[56,57]. For rough surfaces Wenzel[57] presented an equation that relates the
475 contact angle to surface roughness. This model did not use the detail topology of the surfaces but
476 the measured static contact angles are proved to be good approximation of the surface structure. It
477 was not possible to see the flow behaviour between protrusions/grooves but the model was capable
478 of capturing the main flow behaviour.

479 The observed complexity in the structure of the leaves shows that an explicit geometrical model
480 of the leaf structure could improve the accuracy of this model that mainly depended on the
481 measured static contact angel. The detail explicit geometric model of the surface can be developed
482 from high resolution images of the leaves. There are some studies that used simpler geometric

483 feature of the surfaces for developing such VOF model[58,59]. However, such an explicit geometric
484 model needs more computational resource and time. Introducing the dynamic contact angle instead
485 of the static contact angle could further increase the model prediction accuracy. The method of
486 calculated the dynamic contact angle from the measured static contact angle and contact line
487 velocity can be found in Šikalo et al.[51].

488 *3.6. Relevance of the study for improving the performance of spraying systems*

489 The study gives better understanding about the dynamics and possible outcomes of spray
490 droplet impact on plant surfaces. It is observed that the impact behaviour of droplets on a plant
491 surface is a complex process which is controlled by many parameters. It is impossible to get such
492 a detailed information about the impact dynamics of individual droplet in full scale spray
493 applications where a large number of droplets are impacting on a plant surface within a short time.
494 Understanding the physics at droplet scale could help in maximizing the retention of spray droplets
495 on plant surfaces, and improve the performance of spraying systems [3,12]. Better knowledge of the
496 impact dynamics of the droplets on plant surfaces is the basis for the development of precision
497 spraying systems.

498 Several previous studies reported the effect of the different parameters on the impact behaviour
499 of the droplet on solid surfaces. Courbin et al.[60] stated that the dynamics of the wetting process
500 depends on droplet contact angle, droplet shape and surface roughness. Xu et al.[61] conducted an
501 experimental study of droplet splashing in relation to surface roughness, surface texture pattern,
502 surrounding air pressure and liquid viscosity. Relatively lower surrounding pressure suppressed
503 the splashing tendency of the impacting droplet. Increasing the viscosity of the liquid delayed the
504 splashing process. At lower viscosity range (up to a kinematic viscosity of 0.0035 m^2 s^{-1})
505 increasing the viscosity favours the splashing, whereas at higher viscosity increasing the viscosity

retarded the splashing process. On the textured surfaces, the pillar height was the dominant parameter that affected the splashing behaviour. The study showed that for lower pillar height range (< 18 μm) there was a positive correlation between the roughness height and splashing. However for higher height range, there was a negative correlation between the roughness height and the splashing tendency. Tsai et al.[62] reported that for surfaces with micropatterns the splashing behaviour of droplet was highly dependent on the arrangement of the pillars. It was also possible to control the direction of the splash using the arrangement of the pillars. The experimental result of Courbin et al.[63] showed that it is possible to completely inhibit the splashing by controlling the surface roughness.

The spreading and splashing behaviour of droplets with respect to surface inclination and motion was studied by Bird et al.[64] and Courbin et al.[63]. The tangential part of the impact velocity created asymmetric splashing and either triggered or inhibited splashing on the portion of the droplet. Courbin et al.[63] and Pepper et al.[65] studied the effect of surface deflection upon droplet impact on the splashing behaviour. Reducing the tension in the surface suppressed the splashing behaviour of the droplet. Kwon et al[66] experimentally studied the wettability and impact dynamics of droplets on rice leaves, contact distance of bouncing droplets increased with an increase in tangential Weber number. There was anisotropy in wettability between the longitudinal and transversal directions of the leaves. There was a difference in contact distance, contact angle hysteresis, run-off angle and maximum spreading factor of the droplet between the longitudinal and transverse direction of the leaves. Dong et al.[4] reported the effect of surfactant on the dynamics of droplet leaf surface interaction.

All the above studies showed the complexity of the impact process and the importance of the respective parameters in correctly determining the final fate of the droplet on the plant surface.

529 The presented model can be used to study the effect of different relevant spraying parameters,
530 such as: droplet size and impact velocity, liquid formulation, impact direction, surface orientation,
531 surface wettability, surface structure and surrounding air properties. To take into account the effect
532 of surface deflection, this model should be coupled to fluid-structure interaction model. Such a
533 comprehensive study will give a better understanding about the interaction between spray droplets
534 and plant surfaces and the respective results will be applied to improve the accuracy of the existing
535 stochastic droplet retention and drift models [16–18].

536

537 **4. Conclusion**

538 The paper presented a 3-D multiphase CFD model of spray droplet impact on leaf surfaces
539 using a Volume of Fluid (VOF) approach that was validated using high speed camera experiments.
540 The model was capable of predicting successfully the dynamic impact behaviour for both
541 hydrophilic and hydrophobic plant surfaces, and captured the spreading, recoiling, bouncing and
542 shattering stages of the droplet impact process of spray droplets from an agricultural spray nozzle
543 under laboratory conditions. The accuracy of the model prediction can be improved by applying
544 the apparent dynamic contact angle instead of the static angle.

545 The boundary lines of the transition from one impact outcome to another (adhere to bounce,
546 adhere to splash, adhere to bounce and bounce to splash) were expressed as a function of *Re* and
547 *Oh*. The correlations were different for different plant surfaces. There is a need to formulate a more
548 general model equation that takes into account the surface roughness and contact angle.

549 The results demonstrated the capability of VOF based 3-D CFD model in predicting the
550 dynamics and outcomes of vertical water droplet impact on horizontal plant surfaces. The model

will be used to study the real condition during the impact of the droplet on plant surfaces. In reality, the droplets are impacting at an angle, the plant surfaces have some roughness, orientation and elasticity and the surrounding air is moving at a certain direction and magnitude. The results of such a comprehensive model will be applied to improve the accuracy of the commonly assumed stochastic droplet collection and drift models.

Acknowledgment

Author Mulugeta Admasu Delele kindly acknowledges funding by a Back to Belgium Grant of the Belgian Federal Science Policy (BELSPO).

References

1 P. Wagner, R. Fürstner, W. Barthlott and C. Neinhuis, *J. Exp. Bot.*, 2003, **54**, 1295–1303.

2 A. L. Yarin, *Annu. Rev. Fluid Mech.*, 2006, **38**, 159–192.

3 M. Massinon and F. Lebeau, *Biotechnol. Agron. Soc. Environ.*, 2013, **17**, 494–504.

4 X. Dong, H. Zhu and X. Yang, *Pest Manag. Sci.*, 2014, **71**, 302–308.

5 G. J. Dorr, D. M. Kempthorne, L. C. Mayo, W. A. Forster, J. a. Zabkiewicz, S. W. McCue, J. a. Belward, I. W. Turner and J. Hanan, *Ecol. Modell.*, 2014, **290**, 94–101.

6 J. A. Tolk, T. A. Howell, J. L. Steiner, D. R. Krieg and A. D. Schneider, *Irrig. Sci.*, 1995, **16**, 89–95.

7 J. Uddin, R. Smith, N. Hancock and J. Foley, in *Australian Irrigation Conference and Exibition 2010: One Water Many Futures*, Sydney, Australia, 2010, pp. 1–10.

8 C. Bassette and F. Bussière, *Agric. For. Meteorol.*, 2008, **148**, 991–1004.

9 E. Baker and G. M. G. Hunt, *New Phytol.*, 1986, **102**, 161–173.

10 H. Wang, H. Shi, Y. Li and Y. Wang, *PLoS One*, 2014, **9**, e107062.

11 I. K. Zwertvaegher, M. Verhaeghe, E. Brusselman, P. Verboven, F. Lebeau, M. Massinon, B. M. Nicolaï and D. Nuyttens, *Biosyst. Eng.*, 2014, **126**, 82–91.

12 G. Mercer, W. L. Sweatman, a Elvin, J. Caunce, G. Fulford, S. Harper and R. Pennifold, *Proc. 2006 Math. Study Group. ed. G Wake. pp. 57-85.*, 2007, 57–85.

13 Y. Kang, Q. G. Wang and H. J. Liu, *Agric. Water Manag.*, 2005, **74**, 189–199.

14 M. Massinon and F. Lebeau, *Biosyst. Eng.*, 2012, **112**, 56–64.

15 G. Dorr, J. Hanan, S. Adkins, A. Hewitt and B. Noller, *Funct. Plant Biol.*, 2008, **35**, 988–996.

16 A. T. Duga, D. Dekeyser, K. Ruysen, D. Bylemans, D. Nuyttens, B. M. Nicolai and P. Verboven, *Boundary-Layer Meteorol.*, 2015, **157**, 517–535.

17 T. Duga, K. Ruysen, D. Dekeyser, D. Nuyttens, D. Bylemans, B. M. Nicolai and P. Verboven, *Crop Prot.*, 2015, **67**, 200–213.

18 A. M. Endalew, C. Debaer, N. Rutten, J. Vercammen, M. A. Delele, H. Ramon, B. M. Nicolaï and P. Verboven, *Agric. For. Meteorol.*, 2010, **150**, 1383–1392.

19 W. A. Forster, M. O. Kimberley and J. A. Zabkiewicz, *Trans. Am. Soc. Agric. Eng.*, 2005, **48**, 1321–1330.

20 V. Bergeron, J. Y. Martin and L. Vovelle, *Agro Food Ind. Hi. Tech.*, 1999, **10**, 21–23.

21 W. C. Schou, W. A. Forster, G. N. Mercer, M. E. Teske and H. W. Thistle, *Trans. ASABE*, 2012, **55**, 2059–2066.

22 M. Massinon, B. Dumont, N. De Cock, S. O. T. Salah and F. Lebeau, *Crop Prot.*, 2015, **78**, 63–71.

23 C. Richard Glass, K. F. A. Walters, P. H. Gaskell, Y. C. Lee, H. M. Thompson, D. R. Emerson and X. J. Gu, *Pest Manag. Sci.*, 2010, **66**, 2–9.

24 P. R. Gunjal, V. V. Ranade and R. V. Chaudhari, *AIChE J.*, 2005, **51**, 59–78.

25 G. Strotos, M. Gavaises, A. Theodorakakos and G. Bergeles, *Int. J. Heat Mass Transf.*, 2008, **51**, 4728–4742.

26 I. Malgarinos, N. Nikolopoulos, M. Marengo, C. Antonini and M. Gavaises, *Adv. Colloid Interface Sci.*, 2014, **212**, 1–20.

27 S. F. Lunkad, V. V. Buwa and K. D. P. Nigam, *Chem. Eng. Sci.*, 2007, **62**, 7214–7224.

28 H. Fujimoto, Y. Shiotani, A. Y. Tong, T. Hama and H. Takuda, *Int. J. Multiph. Flow*, 2007, **33**, 317–332.

29 H.-C. Wu, W.-S. Hwang and H.-J. Lin, *Mater. Sci. Eng. A*, 2004, **373**, 268–278.

30 J. Y. Li, Q. Han, Y. J. Zhao and X. F. Yuan, *Adv. Mater. Res.*, 2011, **354-355**, 579–584.

31 S. V. Minov, F. Cointault, J. Vangeyte, J. G. Pieters and D. Nuyttens, *Crop Prot.*, 2015, **69**, 18–27.

32 C. W. Visser, P. E. Frommhold, S. Wildeman, R. Mettin, D. Lohse and C. Sun, *Soft Matter*, 2015, **11**, 1708–1722.

33 G. Lagubeau, M. a. Fontelos, C. Josserand, A. Maurel, V. Pagneux and P. Petitjeans, *J. Fluid Mech.*, 2012, **713**, 50–60.

34 T. Mao, D. Kuhn and H. Tran, *AIChE J.*, 1997, **43**, 2169–2179.

35 J. Fukai, Y. Shiiba, T. Yamamoto, O. Miyatake, D. Poulikakos, C. M. Megaridis and Z. Zhao, *Phys. Fluids*, 1995, **7**, 236–247.

36 D. W. Scheller, B. L. and Bousfield, *AIChE J.*, 1995, **41**, 1357–1367.

37 A. Asai, M. Shioya, S. Hirasawa and T. Okazaki, *J. Imaging Sci. Technol.*, 1993, **37**, 205–207.

38 C. Mundo, M. Sommerfeld and C. Tropea, *Int. J. Multiph. Flow*, 1995, **21**, 151–173.

39 S. S. Yoon, P. E. Desjardin, C. Presser, J. C. Hewson and C. T. Avedisian, *Int. J. Multiph. Flow*, 2006, **32**, 132–157.

40 R. L. Vander Wal, G. M. Berger and S. D. Mozes, *Exp. Fluids*, 2006, **40**, 53–59.

41 J. U. Brackbill, D. B. Kothe and C. Zamach, *J. Comput. Phys.*, 1992, **100**, 335–354.

42 J. Eggers, M. a. Fontelos, C. Josserand and S. Zaleski, *Phys. Fluids*, 2010, **22**, 062101.

43 R. Rioboo, M. Marengo and C. Tropea, *Exp. Fluids*, 2002, **33**, 112–124.

44 S. T. Thoroddsen, T. G. Etoh, K. Takehara, N. Ootsuka and Y. Hatsuki, *J. Fluid Mech.*, 2005, **545**, 203–212.

45 W. Bouwhuis, R. C. A. Van Der Veen, T. Tran, D. L. Keij, K. G. Winkels, I. R. Peters, D. Van Der Meer, C. Sun, J. H. Snoeijer and D. Lohse, *Phys. Rev. Lett.*, 2012, **109**, 2–5.

46 R. C. A. van der Veen, M. H. W. Hendrix, T. Tran, C. Sun, P. A. Tsai and D. Lohse, *Soft Matter*, 2014, **10**, 3703–3707.

47 S. Mandre, M. Mani and M. P. Brenner, *Phys. Rev. Lett.*, 2009, **102**, 4–7.

48 M. Mani, S. Mandre and M. P. Brenner, *J. Fluid Mech.*, 2010, **647**, 163–185.

49 L. Xu, W. W. Zhang and S. R. Nagel, *Phys. Rev. Lett.*, 2005, **94**, 1–4.

50 E. Villermaux and B. Bossa, *J. Fluid Mech.*, 2011, **668**, 412–435.

51 S. Šikalo, H.-D. Wilhelm, I. V. Roisman, S. Jakirlić and C. Tropea, *Phys. Fluids*, 2005, **17**, 062103.

52 D. G. K. Aboud and A.-M. Kietzig, *Langmuir*, 2015, **31**, 10100–10111.

53 C. Clanet, C. Béguin, D. Richard and D. Quéré, *J. Fluid Mech.*, 2004, **517**, 199–208.

54 M. Bussmann, S. Chandra and J. Mostaghimi, *Phys. Fluids*, 2000, **12**, 3121–3132.

55 H. Marmanis and S. T. Thoroddsen, *Phys. Fluids*, 1996, **8**, 1344–1346.

56 D. Quéré, *Phys. A Stat. Mech. its Appl.*, 2002, **313**, 32–46.

57 Robert N. Wenzel, *Ind. Eng. Chem.*, 1936, **28**, 988–994.

58 A. S. Ellis, F. T. Smith and A. H. White, *Q. J. Mech. Appl. Math.*, 2011, **64**, 107–139.

59 H. B. Parizi, L. Rosenzweig, J. Mostaghimi, S. Chandra, T. Coyle, H. Salimi, L. Pershin, A. McDonald and C. Moreau, *J. Therm. Spray Technol.*, 2007, **16**, 713–721.

60 L. Courbin, J. C. Bird, M. Reyssat and H. A. Stone, *J. physics. Condens. matter*, 2009, **21**, 1–13.

61 L. Xu, *Phys. Rev. E 75*, 2007, **75**, 1–8.

62 P. Tsai, R. C. a Van Der Veen, M. Van De Raa and D. Lohse, *Langmuir*, 2010, **26**, 16090–16095.

63 L. Courbin, J. C. Bird and H. A. Stone, *Chaos*, 2006, **16**, 58–59.

64 J. C. Bird, S. S. H. Tsai and H. A. Stone, *New J. Phys.*, 2009, **11**, 1–10.
65 R. E. Pepper, L. Courbin and H. A. Stone, *Phys. Fluids*, 2008, **20**, 1–8.
66 D. H. Kwon, H. K. Huh and S. J. Lee, *Exp. Fluids*, 2014, **55**, 1691.

Table 1. Physical properties of water (T = 293 K) and contact angles for different leaf types

Liquid	Density (kg m^{-3})	Viscosity (Pa s)	Surface tension (N m^{-1})	Contact angle per leaf type (°)			
				Apple	Pear	Leek	Cabbage
Distilled water	1000	0.001	0.073	54.9±6.6	68.1±11.2	113.7±27.4	138.2±13.1

664 Table 2: Calculated maximum spread factor ($\frac{d_m}{D}$) of 300 µm water droplet during impact at 2 m

665 s^{-1} on different leaf surfaces

666

667

Leaf surface	Maximum spread factor ($\frac{d_m}{D}$)	
	CFD prediction	Eqn. (4)
Apple	2.73	2.46
Pear	2.54	2.30
Cabbage	1.87	1.72
Leek	2.07	1.84

Table 3. Predicted and measured critical Weber number for transition from adherence to bounce, adherence to splash/shatter and rebound to splash/shatter

Impact transition behaviour		Plant surface			
		Apple	Pear	Leek	Cabbage
Adherence to bounce	Measured	-	-	1.01	0.07
	Predicted	-	-	2.55	0.25
Adherence to splash/shatter	Measured	159.2	166.7	-	-
	Predicted	128.5	136.8	-	-
Bounce to splash/shatter	Measured	-	-	108.1	116.0
	Predicted	-	-	92.5	99.2

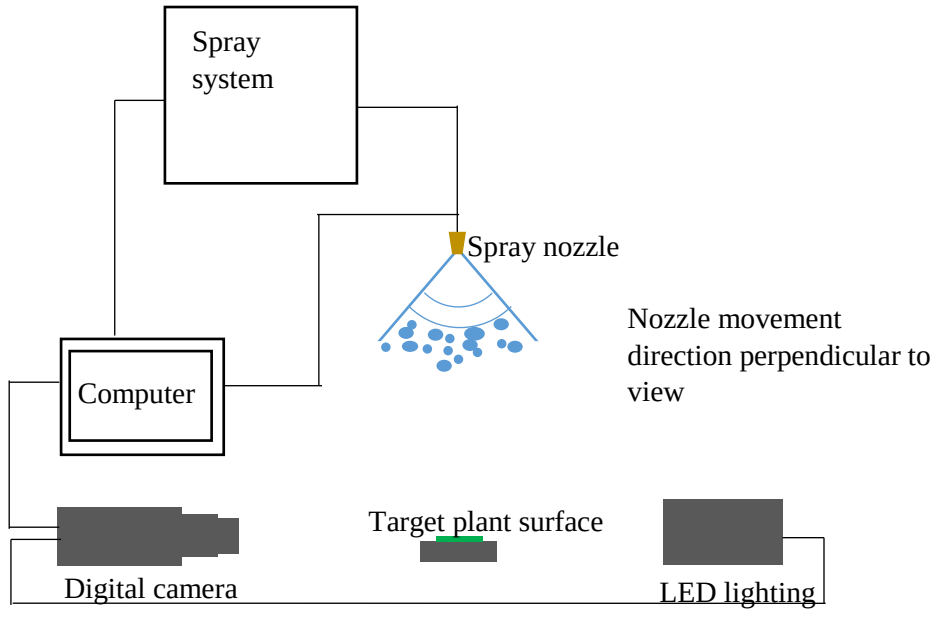

Fig. 1. Experimental set-up for determining droplet impact characteristics

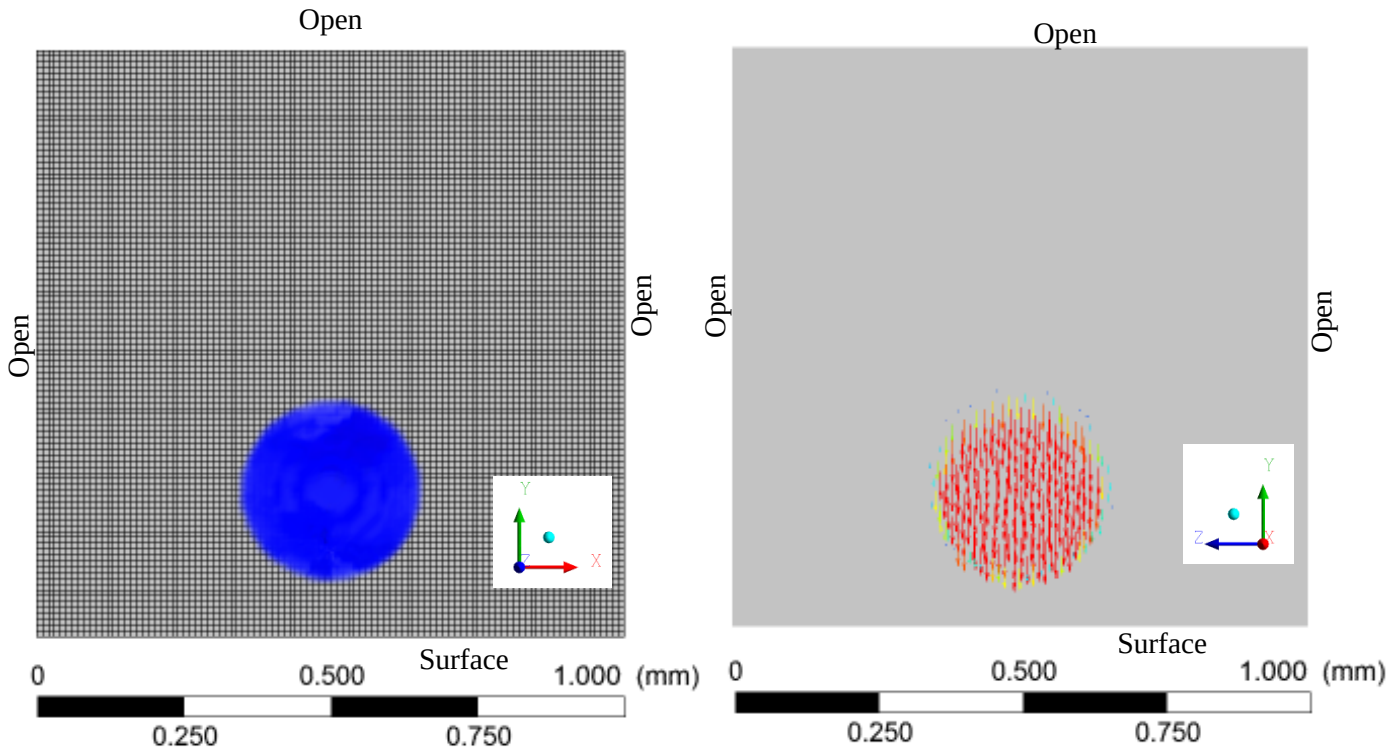

Fig. 2. Typical discretized computational domain showing the initial position of a 300 µm droplet (left), impact velocity vector (right) and the boundary conditions; blue represents a liquid volume fraction of 1; red represents an initial impact velocity of 2 m s^{-1}.

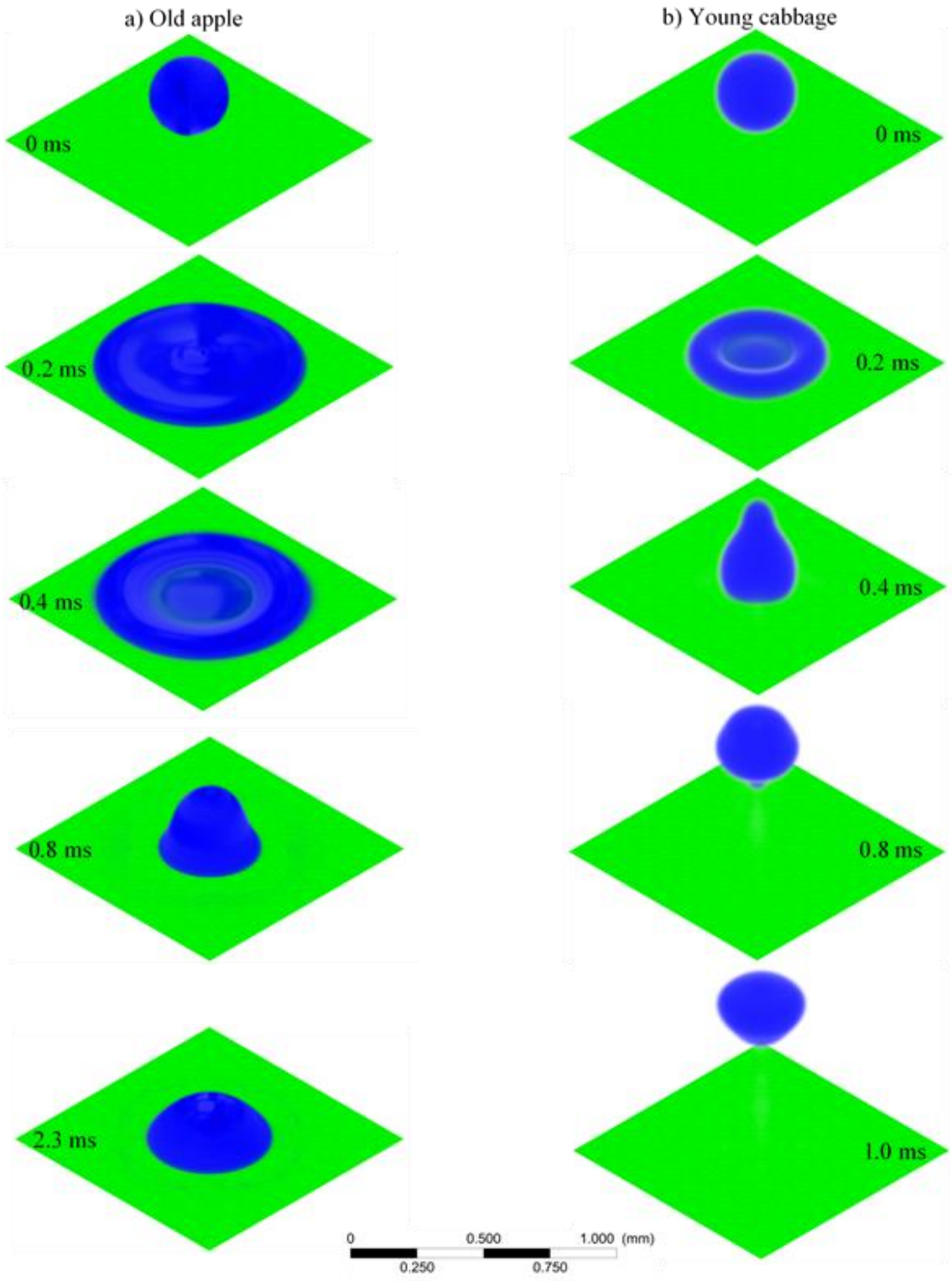

Fig. 3. Predicted dynamic behavior of a 300 µm diameter water droplet during impact on a horizontally placed leaf of (a) old apple and (b) young cabbage with a vertical impact velocity of 2 m s^{-1}; blue represents liquid volume fraction of 1 and the time after impact is given in milliseconds

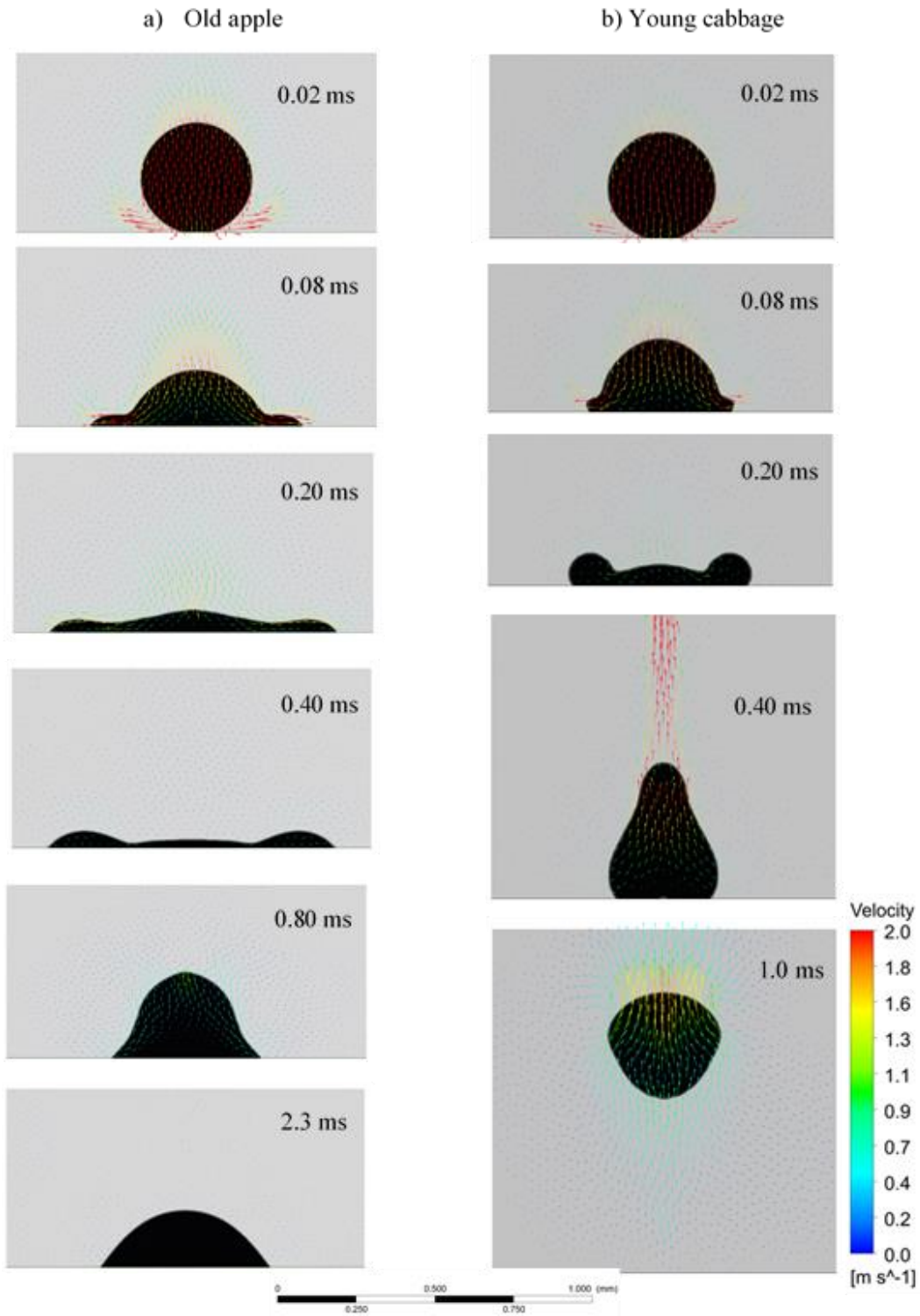

Fig. 4. Predicted dynamic behavior and VOF velocity distribution during droplet impact on a horizontally placed leaf of (a) old apple and (b) young cabbage with a vertical impact velocity of 2 m s^{-1}; the black color represents the contour of the droplet; the time after impact is given in milliseconds

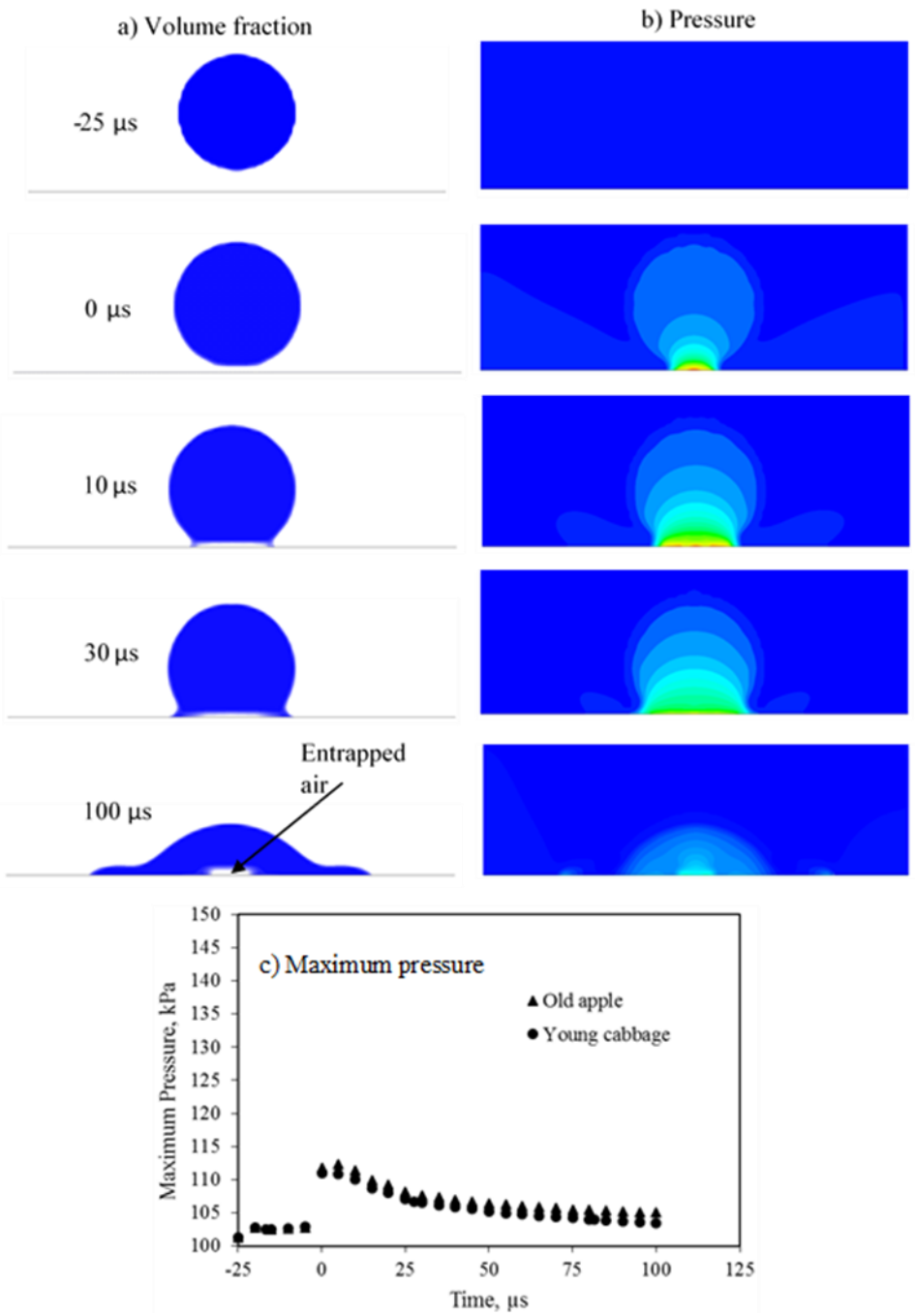

Fig. 5. Predicted dynamic behavior of (a) air entrapment: blue represents liquid volume fraction of 1, (b) pressure distribution: blue and red represent pressure of 101.3 kPa and 112.4 kPa, respectively, (c) maximum pressure; after the impact of 300 µm water droplet on horizontal leaf surface at a vertical velocity of 2 m s^{-1}, 0 µs is the calculated collision time of the injected droplet to the surface (from the initial injection velocity and position)

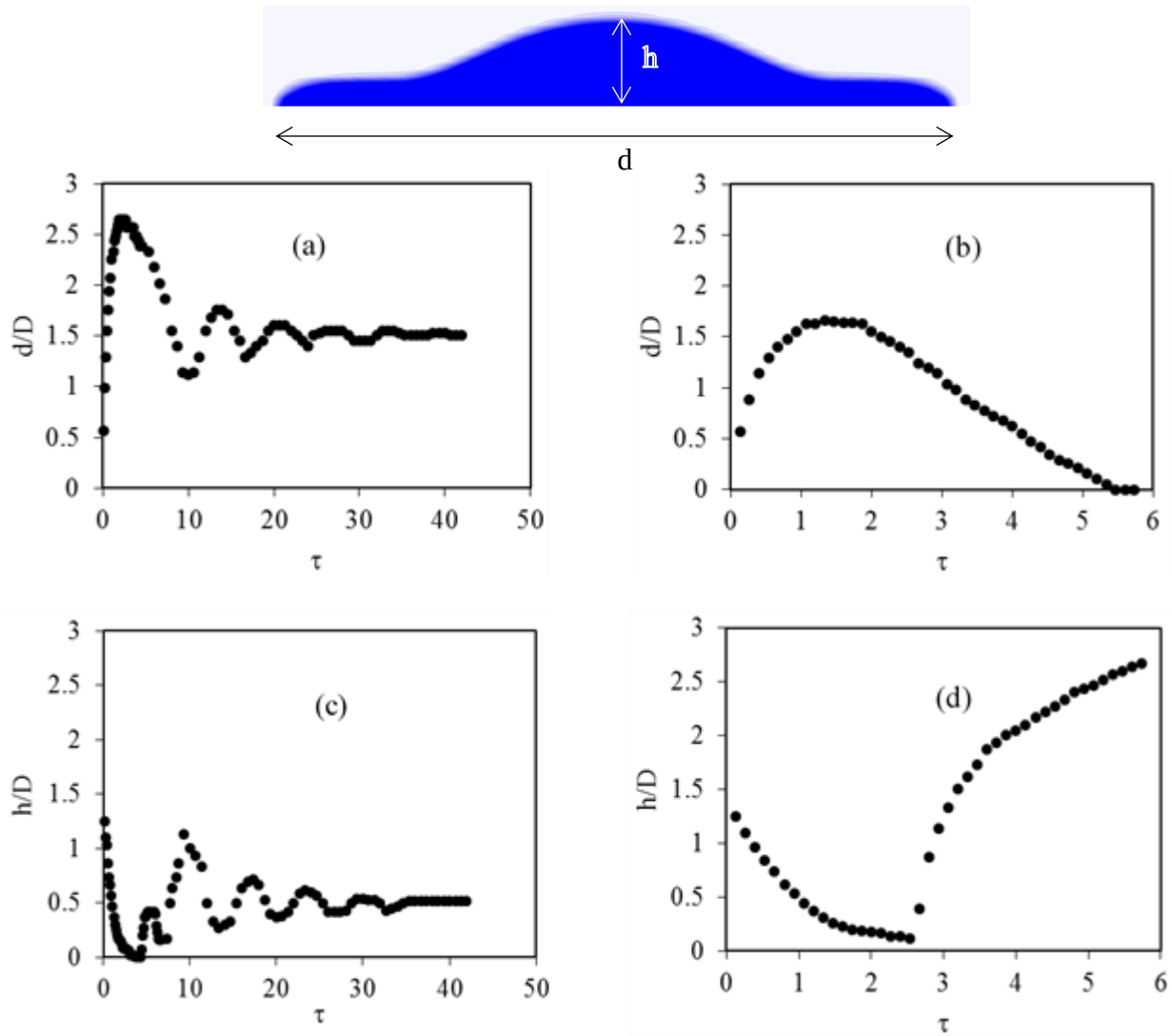

Fig. 6. Predicted time evolution of droplet spread diameter (*d*) and height (*h*) after impact for a 300 µm water droplet at a vertical impact velocity of 2 m s^{-1} on a horizontally placed old apple (a, c) and young cabbage leaf (b, d): (a) and (b) present the dimensionless droplet spread diameter; (c) and (d) the dimensionless droplet height (*h/D*) as a function of dimensionless time (τ). *h* represents the distance between the top of the drop and the solid surface

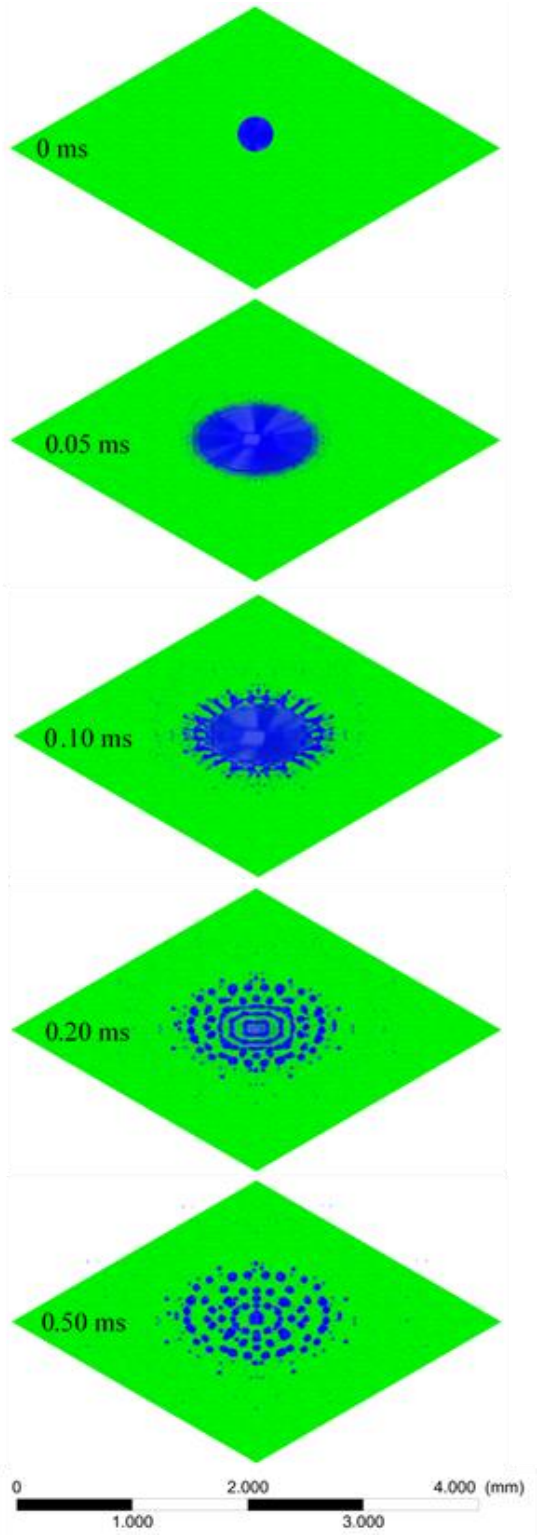

Fig. 7. Predicted dynamic behavior of a 300 µm water droplet after impact on a horizontally placed young cabbage leaf at a vertical velocity of 10 m s^{-1}; blue represents a liquid volume fraction of 1 and the time after impact is given in milliseconds

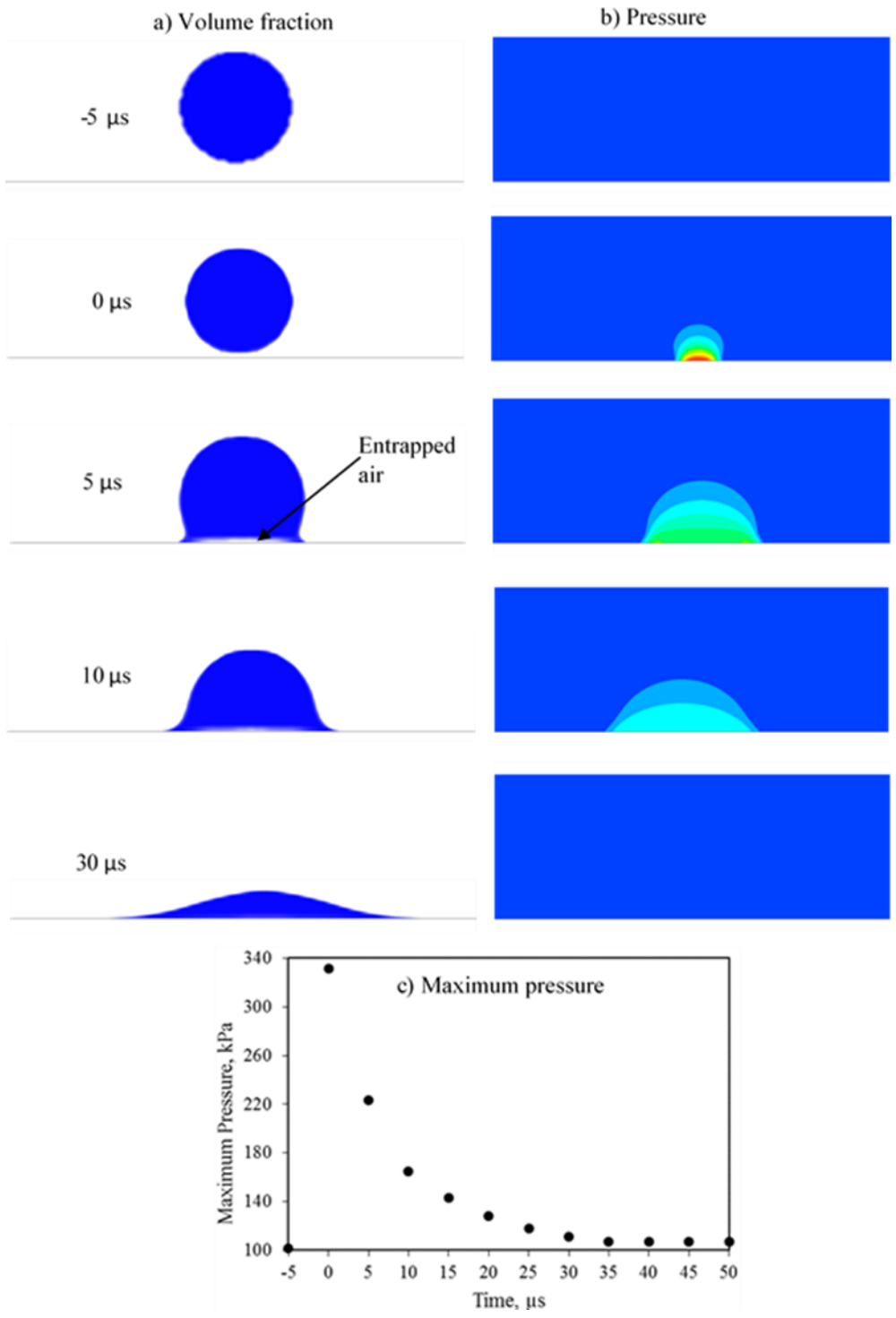

Fig. 8. Predicted dynamic behavior of (a) air entrapment: blue represents liquid volume fraction of 1, (b) pressure distribution: blue and red represent pressure of 101.3 kPa and 331.1 kPa, respectively, (c) maximum pressure; after the impact of 300 µm water droplet on horizontal young cabbage leaf surface at a vertical velocity of 10 m s^{-1}, 0 µs is the calculated collision time of the injected droplet to the surface (from the initial injection velocity and position)

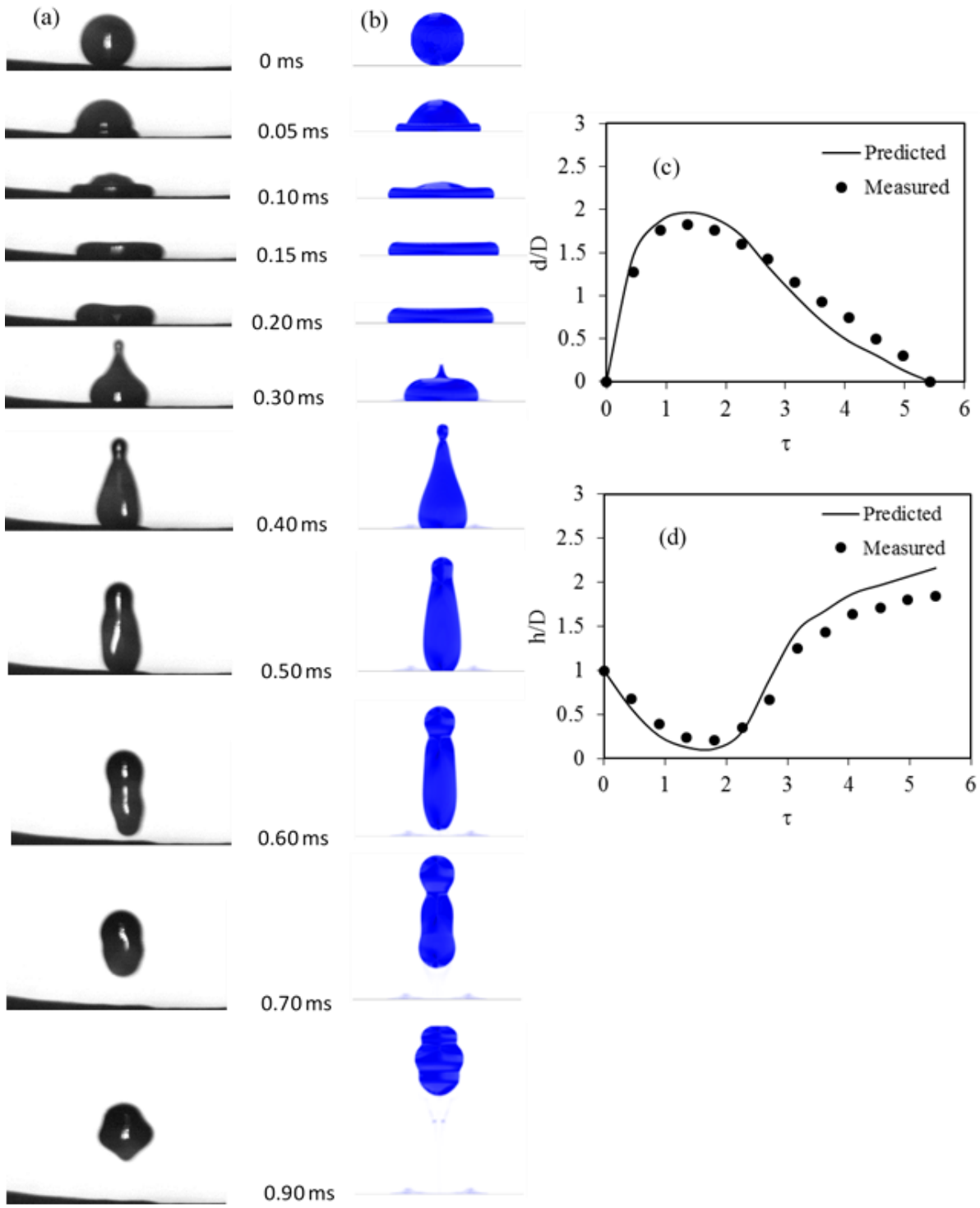

743

744 Fig. 9. Comparison between measured and predicted dynamic behavior of a 310 µm water droplet
745 after impact on horizontal young cabbage leaf at a vertical velocity of 2.8 m s^{-1}; (a) measured
746 shape, (b) predicted shape, (c) predicted and measured dimensionless droplet spread diameter, (d)
747 predicted and measured dimensionless droplet height; blue represents a liquid volume fraction of
748 1 and the time after impact is given in milliseconds

749

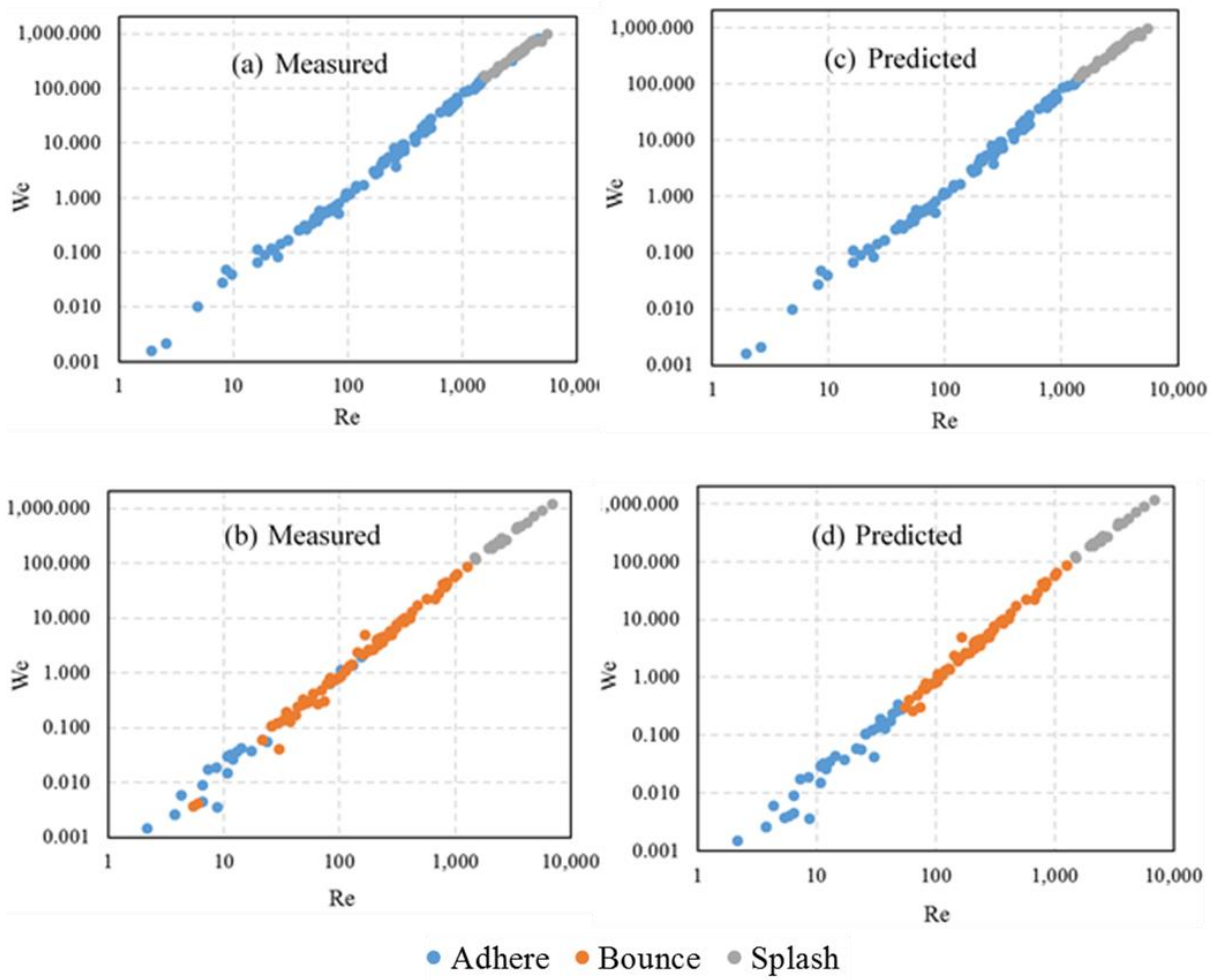

750

751 Fig. 10. Measured and predicted outcome of dynamics of water droplets with different diameter
752 and impact velocity after impact on horizontally placed leaf surfaces; old apple leaf: measured (a)
753 and predicted (b), young cabbage leaf: measured (c) and predicted (d).

754

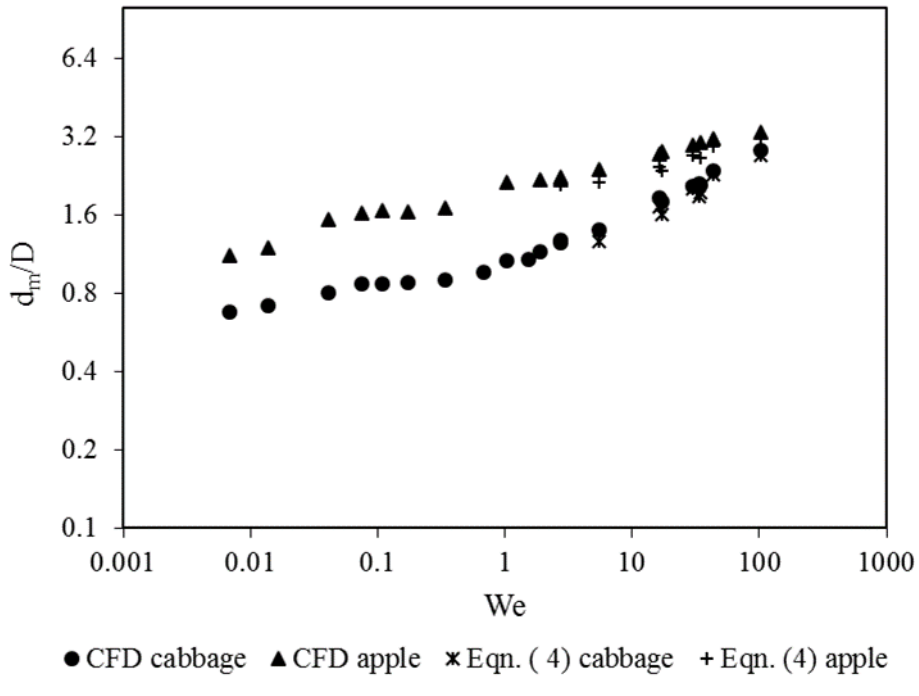

Fig. 11. Predicted maximum spread factor (d_m/D) as a function of Weber number (We) for water droplets, using CFD or resulting from Eqn. (4) on young cabbage and old apple leaves

760

761

762

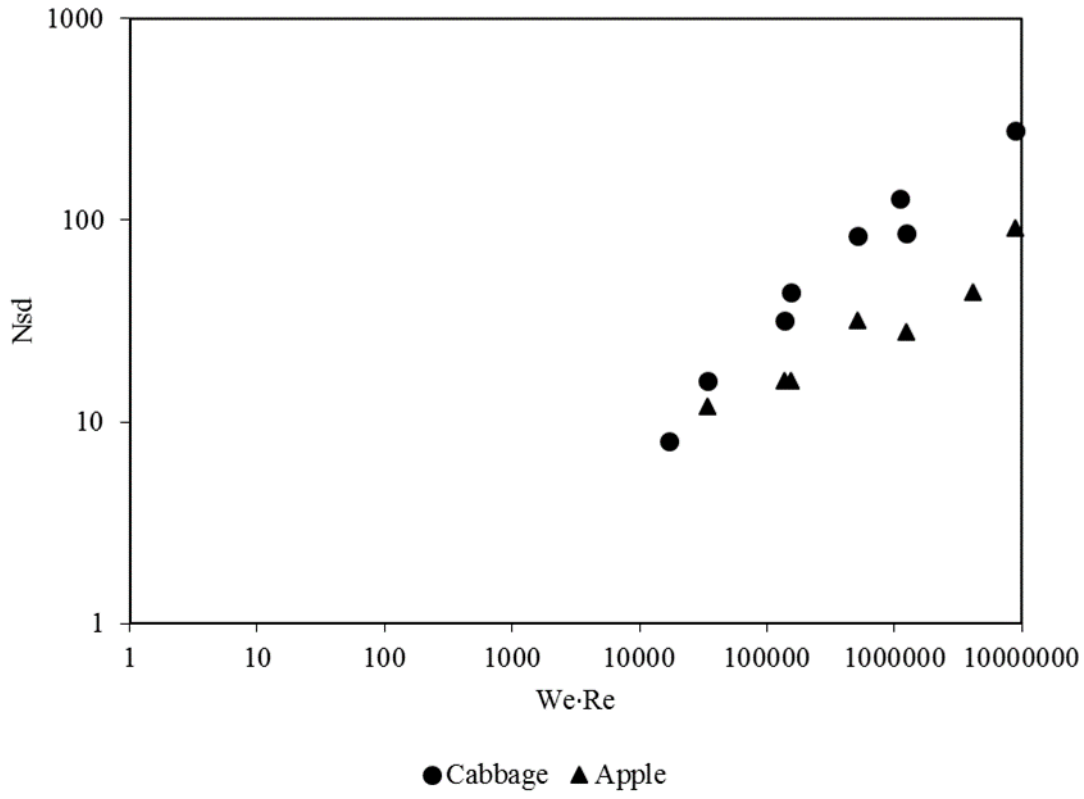

763

764 Fig. 12. Predicted number of secondary droplets (N_{sd}) formed during splashing/shattering of the
765 droplet on young cabbage and old apple leaves as a function of *We·Re*.

766

767

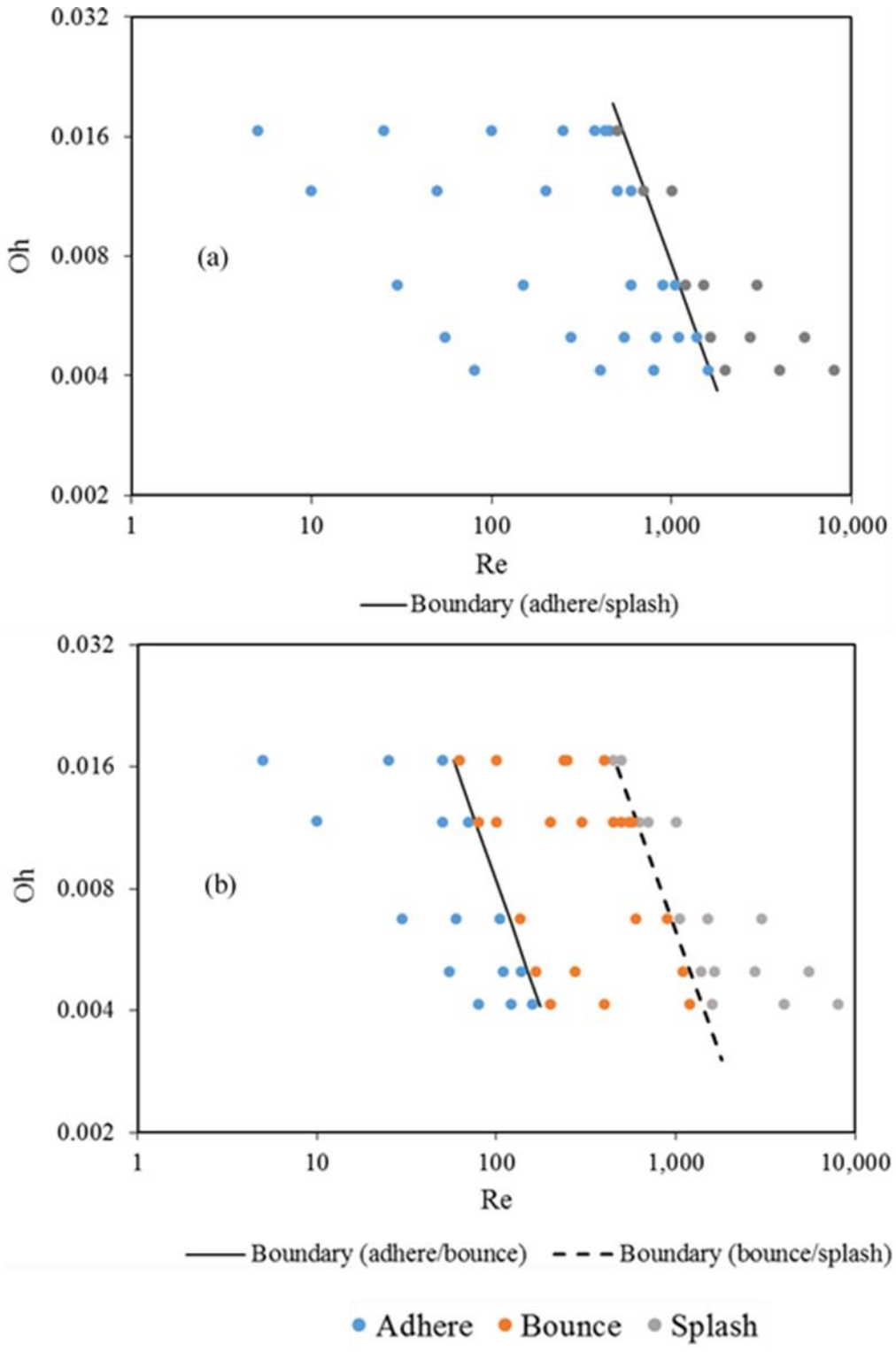

768

769 Fig. 13. Predicted boundary line ($OhRe^{1.25} = K$) between the different droplet impact outputs
770 (adhere, bounce and splash/shatter) on old apple (a) and young cabbage (b) leaves as a function
771 of Reynolds (*Re*) and Ohnesorge (*Oh*) numbers

772

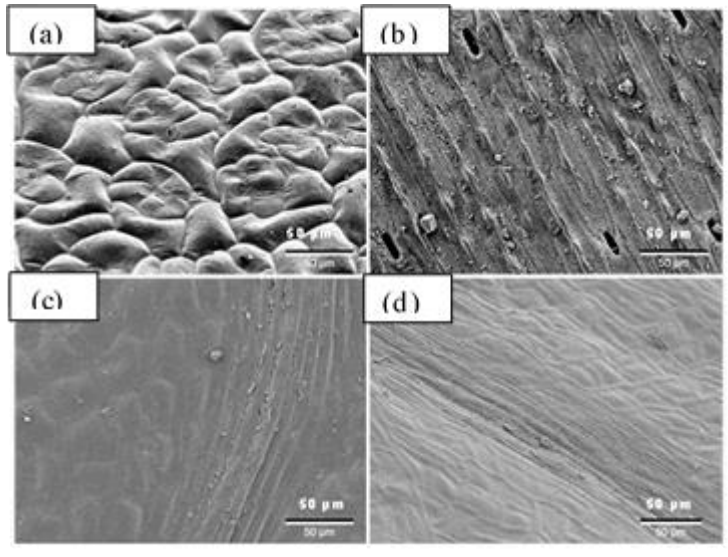

773

774 Fig. 14. SEM images of different leaf surfaces: (a) cabbage (*Brassica oleracea*); (b) leek (*Alium*
775 *ampeloprasum var porrum*); (c) apple (*Malus domestica*); (d) pear (*Pyrus communis*)

776

777

778